Gas-Phase Nucleation in the Tetraethylorthosilicate (TEOS)/O_3 APCVD Process

Kikuo Okuyama, Toshiyuki Fujimoto and Tadao Hayashi
Dept. of Chemical Engineering, Hiroshima University, Higashi-Hiroshima 739, Japan

Motoaki Adachi
Research Institute for Advanced Science and Technology, Osaka Prefecture University, Sakai 593, Japan

The chemical reaction mechanism and fine particle generation during atmospheric pressure chemical vapor deposition with the tetraethylorthosilicate/ozone system were studied experimentally and theoretically for a flow-type vertical-tube reactor. For the thermal decomposition of ozone, numerical simulations obtained using reaction rate constants for a batch reactor explained experimental results well. The activation energy of chemical reaction between TEOS and the oxygen radical, $O\cdot$, was evaluated from the particle generation rate (2.18×10^5 J/mol). Particle population balance equations, based on the simplified reaction coagulation model, were coupled with equations for the thermal decomposition of ozone and chemical transformations of TEOS and solved numerically. Calculation results for particle number concentration and size agreed with experimental results for temperatures below 430 K. For temperatures above 430 K measured concentrations agreed well with calculated values, but measured sizes were significantly smaller than calculated sizes. Thermal desorption spectra from particles generated at 423 K revealed a peak from C_2H_4 at ~ 800 K, presumably from ethoxy groups. This emission explains, at least in part, the observed decrease in particle size at high temperatures.

Introduction

Silicon dioxide film preparation by atmospheric pressure chemical vapor deposition (APCVD) from tetraethylorthosilicate (TEOS) is used extensively in very large-scale integration (VLSI) technology for constructing multilevel interconnections of deep submicron layers, because the prepared films show a flow-like shape. TEOS, $Si(O\text{-}C_2H_5)_4$, is an alkoxide of silicon and is widely used as a silicon source in CVD. Figure 1 shows both conformal and flow-like films prepared by the TEOS/O_3 APCVD process. Conformal films grow at the same rate in all directions and are formed when ozone concentrations are low. The flow-like films show nonconformal growth, flowing from the upper corner to the lower corner of steps, and tend to form at high ozone concentrations. This liquid-like characteristic causes filling of deep-submicron gaps and planarization of the film. The TEOS/O_3 APCVD process is particularly advantageous for low-temperature film formation, has self-planarization and excellent gap-filling properties, and is suitable for formation of interlayer dielectric films after wiring by low melting point metals such as aluminum. Previous studies of film formation in this system have been reported. Adams and Capio (1979) studied the deposition of silicon dioxide films at reduced pressure and high temperature. Fujino et al. (1990, 1991, 1992) studied the deposition rate and properties of silica films produced by APCVD using the TEOS/O_3 chemical system. Matsuura et al. (1991) measured deposition rate and film characteristics of thin films deposited by APCVD using several organic silicon compounds including TEOS and OMCTS (octamethylcyclotetrasiloxane; $[(CH_3)_2Si\text{-}O\text{-}]_4$) and ozone. Kawahara et al. (1992) measured the decomposition process of TEOS using *in-situ* FT-IR. Adachi et al. (1992–1996) found the relationship between the chemical structures of nanometer-sized particles and the resulting film morphology.

Correspondence concerning this article should be addressed to K. Okuyama.

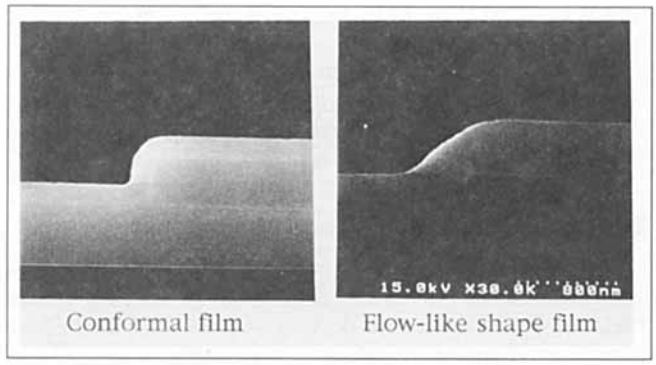

Figure 1. Scanning electron microscopy of conformal and flowlike films deposited on the Si wafer with step.

In the $TEOS/O_3$ APCVD process, silica films are prepared at temperatures below 573 K. The formation of films at such low temperatures in this system is possible due to the presence of the highly reactive oxygen radical, which is formed by the thermal decomposition of ozone. Because oxygen radicals initiate chemical reactions, the distribution of oxygen radicals must be understood before one can model the film formation mechanism. However, it is very difficult to measure the oxygen radical concentration and the mechanism of film formation is still not well understood.

Figure 2 illustrates the mechanisms of thin film growth and particle formation in a $TEOS/O_3$ APCVD reactor. TEOS vapor reacts with oxygen radicals produced by the thermal decomposition of ozone to form intermediate species in the gas phase. These intermediates deposit on the silicon wafer where they undergo surface reactions, such as polymerization, to form a silicon dioxide film. Simultaneously, gas-phase intermediate species with very low vapor pressures form liquid-like droplets by homogeneous nucleation that polymerize in the gas-phase to become silica-like particles. In most film preparation processes, the deposition of such particles on the substrate causes contamination. We hypothesize that at low temperatures, the nanometer-sized particles are generated by coagulation of intermediates, and that they retain the composition of the intermediates at the exit from the reaction. Therefore, the rate of particle production and the particle composition reflect the chemical production and composition of the intermediates.

In this work, we carried out experimental measurements and numerical simulations of the processes in a simple vertical-tube CVD reactor to explore the mechanism and rate of gas-phase reactions and particle generation in the $TEOS/O_3$ system. Similar analysis for other systems have been reported previously. Okuyama et al. (1991) studied particle formation in SiO_2 film formation by reaction of $SiCl_4$ and O_2 and particle formation by oxidation of metal alkoxide (Okuyama et al., 1986, 1990). Whitby and Hoshino (1996) simulated particle formation in a SiH_4:O_2:He low-pressure CVD reactor, and compared their results with measured particle sizes.

In principle, numerical simulations of particle formation in such systems involve simultaneous solutions to the equations for fluid flow, heat transfer, reaction kinetics, and particle nucleation and growth. In this study we assume that the fluid flow and temperature field are unaffected by chemical transformations. Therefore, we first solve for local velocities and temperatures, and use these to solve the coupled equations for gas-phase reactions and particle formation. We use the simplified reaction coagulation (SRC) model proposed by Wu

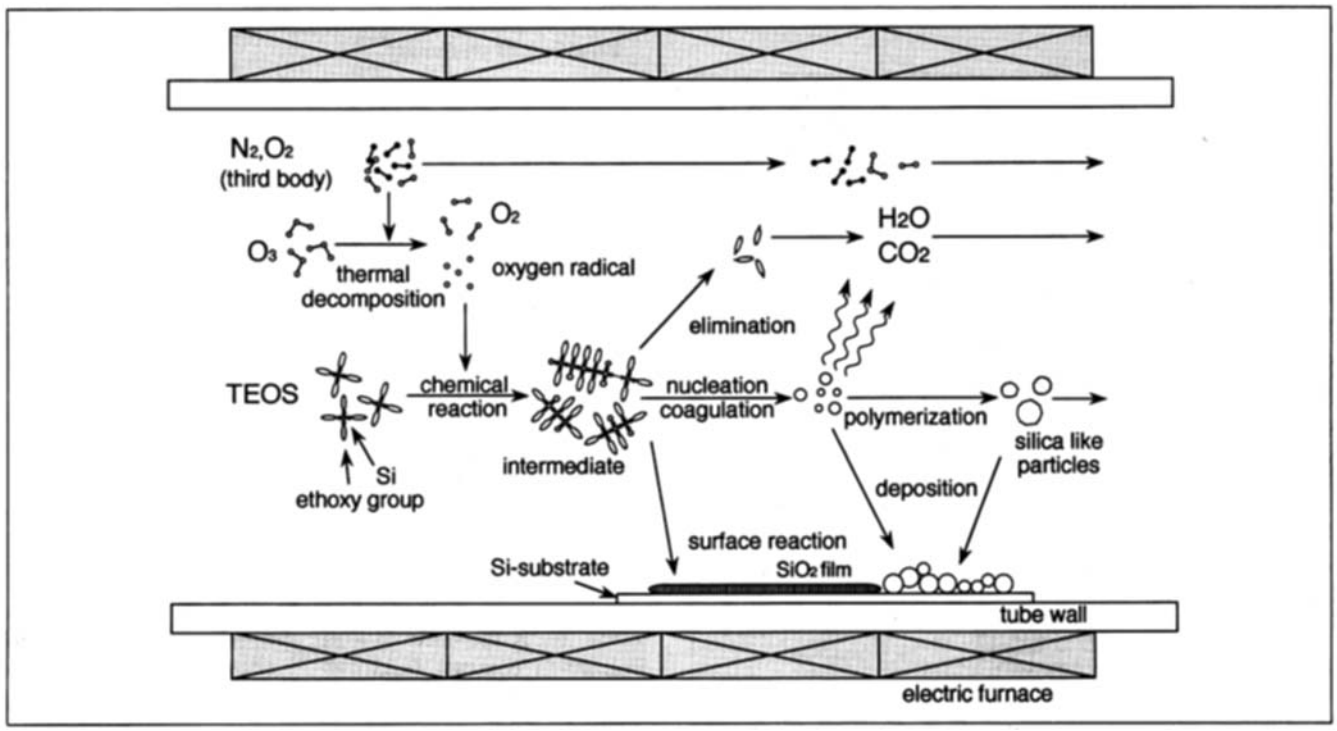

Figure 2. Particle and thin film formation in the $TEOS/O_3$-APCVD reactor.

et al. (1988) for particle nucleation and growth. The SRC model requires much less computational overhead than other schemes (such as Wu and Flagan, 1988, discrete-sectional model) that have been developed for solving the general dynamic equation for aerosols (Gelbard and Seinfeld, 1979), yet adequately captures the details of cluster formation and growth that are essential for simulating nucleation.

Experimental Apparatus and Method

Figure 3 shows the experimental apparatus. This system consisted of an infusion pump for delivering TEOS at a known rate, a temperature controlled TEOS evaporator, and a tube-type CVD reactor. Diagnostic tools included an ozone monitor (DYLEC Co. Ltd., Model DY-1500) for measuring concentrations at the inlet and outlet of the tube furnace, a DMA (TSI Inc., Model 3071), and a CNC (TSI Inc., Model 3020) for measuring particle size and number concentration. The reactor was a vertical quartz tube with an inner diameter of 13, 20 or 30 mm, and was heated by a six-zone electric furnace. In this study, the outlet temperature was maintained at room temperature to allow measurement of the ozone concentration and particle distributions. Measurements of ozone thermal decomposition were carried out for two temperature distributions. For distribution 1, the lower three heater sections were on and the upper three were off, and for distribution 2 a continuous temperature increase was achieved.

An ozone/oxygen mixture produced from oxygen by a surface-discharge-type ozonizer, was introduced along the axis of the reactor at a flow rate of either 100 or 200 cm^3/min. A second flow containing a mixture of nitrogen and TEOS vapor from the evaporator at a flow rate of either 300 or 600 cm^3/min was mixed with the O_3/O_2 flow at the inlet to the reactor. The total flow rate was fixed at either 400 or 800 cm^3/min. Numerical computations confirm that the two flows mixed completely by diffusion before they entered the furnace.

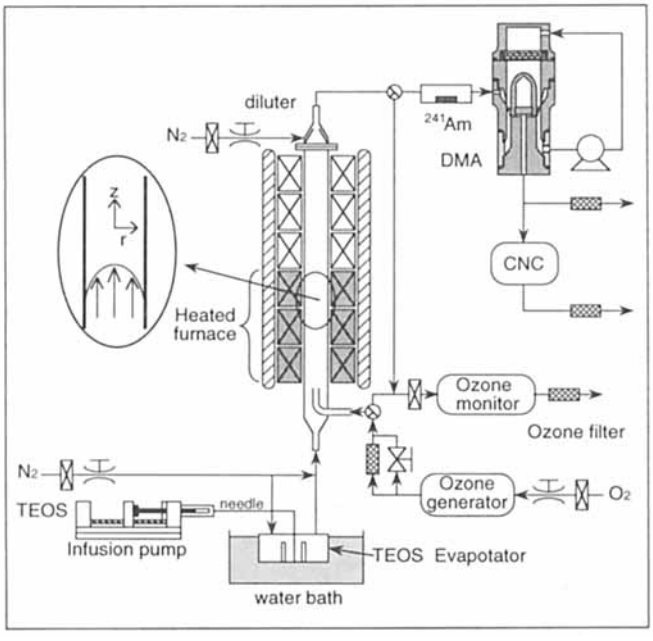

Figure 3. Experimental apparatus for thermal decomposition of ozone and particle generation.

We measured the change in the ozone concentration due to the thermal decomposition of ozone and the particle number concentration and size distribution. The furnace temperature T_f was varied from 298 to 573 K.

Evaluation of Thermal Decomposition of Ozone

The concentrations of oxygen radicals, O_2, O_3, and N_2 within the reactor were determined by numerically solving their respective convective-diffusion equations, including the effects of chemical reactions in the source terms. These equations are of the form

$$\nabla \cdot D\nabla\left(\frac{C}{\rho}\right) - \nabla \cdot \boldsymbol{u}\left(\frac{C}{\rho}\right) - \rho S = 0, \tag{1}$$

where ρ, C, D, S are density (kg/m^2), concentration (mol/L), diffusion coefficient (m^2/s), source term (mol/L·s) of each gas. To solve Eq. 1 for each species, the temperature and velocity distributions within the reactor are needed. In this article, we assume the concentration of ozone was low enough that we could neglect its effect on density, viscosity, heat capacity, thermal conductivity, and so on. We therefore determined the fluid flow and temperature fields by solving the coupled fluid-flow and heat-transfer equations, and used the resulting velocity and temperature fields to solve the convective-diffusion equations for the other chemical species.

Gas velocity and temperature distribution in the flow reactor

The gas velocity and temperature distributions are governed by the following equations. ($\boldsymbol{u}$, u_r, and u_z are defined as the velocity of the carrier gas (m/s).)

Equation of continuity

$$\nabla \cdot (\rho \boldsymbol{u}) = 0 \tag{2}$$

Momentum equation

$$-[\nabla \cdot \rho \boldsymbol{u}\boldsymbol{u}] - \nabla p - [\nabla \cdot \boldsymbol{\tau}] + \rho \boldsymbol{g} = 0 \tag{3}$$

Energy equation

$$\nabla \cdot \alpha \nabla T - \nabla \cdot (\boldsymbol{u} T) = 0 \tag{4}$$

where ρ, α and $\boldsymbol{g}$ in Eqs. 2–4 are the gas density (kg/m^3), the thermal diffusion coefficient (m^2/s) and gravity (m/s^2), respectively. The gas density ρ is assumed to be expressed by the ideal gas law as

$$\rho = p m_g / \kappa T, \tag{5}$$

where m_g is the mass of a gas molecule (kg) and κ is the Boltzmann constant (1.38×10^{-23} J/K). The thermal diffusion coefficient α (m^2/s) is a function of temperature.

The boundary conditions for the gas velocity and the temperature in Eqs. 2–4 are

$$z = 0, \quad 0 \le r < R_T;$$

$$T = T_0, \quad u_z = \frac{2Q}{60\times10^6\,\pi R_T^2}\left[1-\left(\frac{r}{R_T}\right)^2\right], \quad u_r = 0, \quad (6)$$

$$0 < z \le z_{f_1}, \quad r = R_T;$$

$$T = T_w = T_0, \quad u_r = u_z = 0, \quad (7)$$

$$z_{f_1} < z \le z_{f_2}, \quad r = R_T;$$

$$T = T_w = T_0 + (T_f - T_0)\left(\frac{z_{f_2} - z}{z_{f_2} - z_{f_1}}\right), \quad u_r = u_z = 0, \quad (8)$$

$$z_{f_2} < z \le z_{f_3}, \quad r = R_T;$$

$$T = T_w = T_f, \quad u_r = u_z = 0, \quad (9)$$

$$z_{f_3} < z \le Z, \quad r = R_T;$$

$$T = T_w = T_0 + (T_f - T_0)\left(\frac{Z - z}{Z - z_{f_3}}\right)^a, \quad u_r = u_z = 0 \quad (10)$$

and

$$z = Z, \quad 0 \le r < R_T;$$

$$T = T_0, \quad u_z = \frac{2Q}{60\times10^6\,\pi R_T^2}\left[1-\left(\frac{r}{R_T}\right)^2\right], \quad u_r = 0, \quad (11)$$

where T_0 and Q are the temperature (298.15 K) and volumetric flow rate at room temperature (cm^3/m), respectively, of the gas at the reactor inlet; R_T and Z are the inner radius (m) and length (m) of the reactor, respectively; z_{f1} is the position of the start of the furnace, z_{f2} and z_{f3} are the positions of start and end of controlled-temperature section, and T_f, T_w and a are the furnace temperature (K), the wall temperature (K), and a constant determined from the wall temperature measurements, respectively. r is the radial position (m), and z_{f1}, z_{f2}, and z_{f3} are defined as the axial position of heating. The wall temperature profiles along the z-direction shown in Figure 4 are described by Eqs. 6–11 based on the temperature measured with a thermocouple.

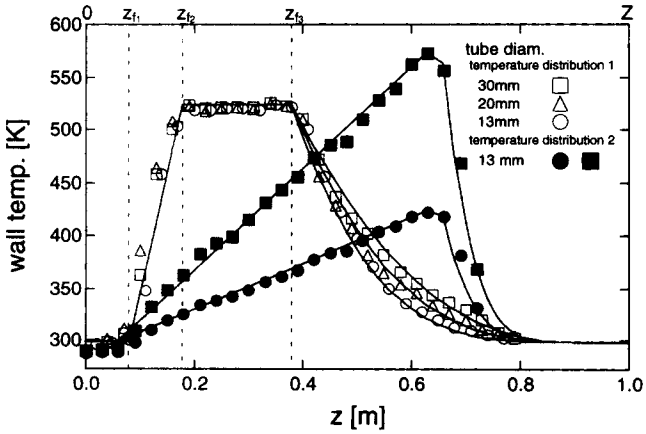

Figure 4. Temperature profiles of the reactor wall measured with a thermocouple.

All equations were discretized using a control volume method and solved using the SIMPLER algorithm (Patankar, 1980). The number of grid points along the r (radial) and z (axial) directions are 13×122, 14×122, and 24×122 for tube diameters of 13, 20 and 30 mm, respectively. In the numerical simulations the influence of buoyancy could have been included by adding the gravity term in Eq. 3. However, we selected experimental conditions where convection was strong enough so that buoyancy could be neglected.

Ozone thermal decomposition mechanism and rate

The source term in Eq. 1 represents the generation and destruction of chemical species, and is derived from the following mechanism and reaction rate constants. The thermal decomposition of ozone in a batch reactor was studied by Benson et al. (1957, 1965) at the temperatures between 90–100°C. Their experiments were carried out in a spherical Pyrex chamber and in an irregularly shaped Pyrex chamber. They developed the following reaction mechanism

$$O_3 + M \xrightarrow{k_1} O_2 + O\cdot + M, \quad (12)$$

$$O_2 + O\cdot + M \xrightarrow{k_2} O_3 + M, \quad (13)$$

and

$$O_3 + O\cdot \xrightarrow{k_3} 2O_2, \quad (14)$$

where M stands for a third body such as O_2, O_3 and N_2. Here, the concentration of M is given by

$$C_M = 2.273C_{O_3} + C_{O_2} + 0.9318C_{N_2}. \quad (15)$$

This expression, based on O_2 gas, was derived by modifying the original experimental relation presented by Benson and Axworthy (1957, 1965). The reaction rate constants are

$$k_1 = 2.02\times10^{12}\exp(-1.00\times10^5/RT), \quad (16)$$

$$k_2 = 2.96\times10^{7}\exp(3.73\times10^3/RT), \quad (17)$$

and

$$k_3 = 3.37\times10^{10}\exp(-2.40\times10^4/RT). \quad (18)$$

Using the above reaction mechanism and reaction rate constants, we derived the following source terms for the convective-diffusion equations

$$r_O = k_1C_{O_3}C_M - k_2C_{O_2}C_OC_M - k_3C_{O_3}C_O, \quad (19)$$

$$r_{O_2} = k_1C_{O_3}C_M - k_2C_{O_2}C_OC_M + 2k_3C_{O_3}C_O, \quad (20)$$

and

$$r_{O_3} = -k_1C_{O_3}C_M + k_2C_{O_2}C_OC_M - k_3C_{O_3}C_O. \quad (21)$$

Table 1. Conditions of Experiments and Numerical Calculations for Thermal Decomposition of Ozone

Run number	1	2	3	4	5	6	7
Tube diameter (mm)	13	20	30	13	13	13	13
Flow rate (cm^3/min)	400	400	400	800	400	400	400
Init. ozone conc. (mol/L)	8.50×10^{-5}	8.50×10^{-5}	8.50×10^{-5}	8.50×10^{-5}	1.70×10^{-4}	4.30×10^{-5}	8.50×10^{-5}
Temp. distribution	1	1	1	1	1	1	2

Experimental and calculation results on the thermal decomposition of ozone

The conditions of our experiments and numerical simulations are shown in Table 1. Run No. 1 corresponds to standard operating conditions. In Run Nos. 2 and 3, the diameter of reactor tube was increased from 13 mm to 20 and 30 mm, respectively, while in Run No. 4, the gas-flow rate was changed from 400 to 800 cm^3/min. In Run Nos. 5 and 6, the initial ozone concentration was changed from 8.5×10^{-5} mol/L to 1.7×10^{-4} and 4.3×10^{-5} mol/L, respectively. For these experiments, the temperature of the heated zone of the reactor was kept constant (temperature distribution 1) and the temperature profiles are shown by the open circles, triangles, and squares in Figure 4. In Run No. 7, the temperature profiles shown by solid circles in Figure 4 were used. As seen in Figure 5 the ozone concentration measured at the exit of the reactor agreed well with the calculated results for all cases. This agreement indicates that our simulation results for the thermal decomposition of ozone are reliable.

Figure 6 shows the mixing-cup temperature and the concentration profiles for ozone and oxygen radicals predicted by the numerical simulations for an initial ozone concentration of 8.5×10^{-5} mol/L, a reactor diameter of 13 mm, and a volumetric flow rate of 400 cm^3/min. In order to simplify the treatment of the thermal expansion of the gas, the concentration is expressed in terms of the mass fraction. The ozone concentration did not vary significantly in the axial direction at 373 and 423 K. Above 473 K, however, the ozone concentrations decreased in the heated zone and reached a constant value at the end of the heated zone.

The oxygen radical concentration behaved similar to the temperature profile. At temperatures below 473 K, the oxygen radical concentration reached a constant value in the heated zone and decreased after the end of the heated zone. At 523 and 573 K, the concentration reached a maximum at the start of the heated zone and then decreased slightly. The oxygen radical concentrations continued to decrease after the end of the heated zone. The maximum oxygen radical concentration at 573 K is about two orders of magnitude higher than at 473 K. If T_f is high enough to decompose ozone, the concentration of oxygen radicals also decreases. We believe this explains the decrease in the film growth rates for temperatures above 573 K.

Evaluation of Particle Generation

Figures 7a and 7b show typical experimental results for number concentrations and volumetric average diameters, respectively, for particles generated at various temperatures. Figure 8 shows the particle-size distributions. At temperatures below 380 K, the number concentration increases exponentially with increasing furnace temperature, but at higher temperatures, the number concentration reaches an asymptotic value.

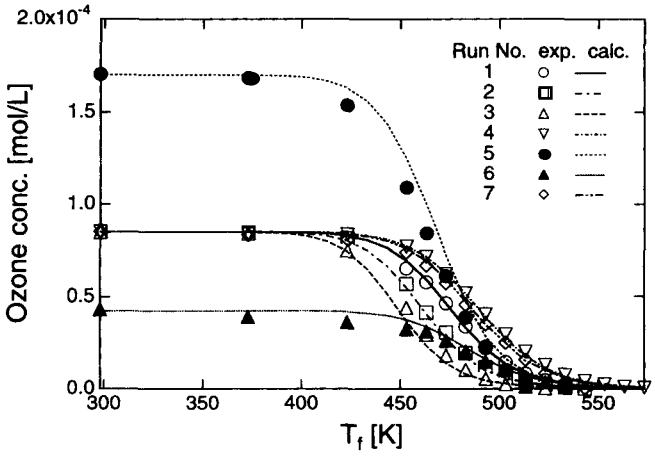

Figure 5. Measured vs. calculated ozone concentrations at various reactor temperatures.

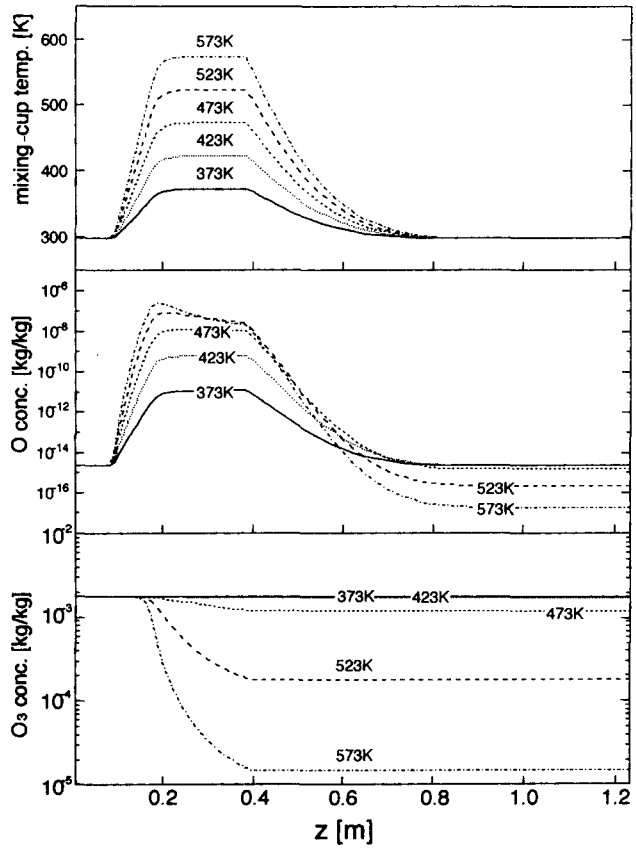

Figure 6. Calculated axial mixing-cup temperatures and concentrations of ozone and oxygen radical.

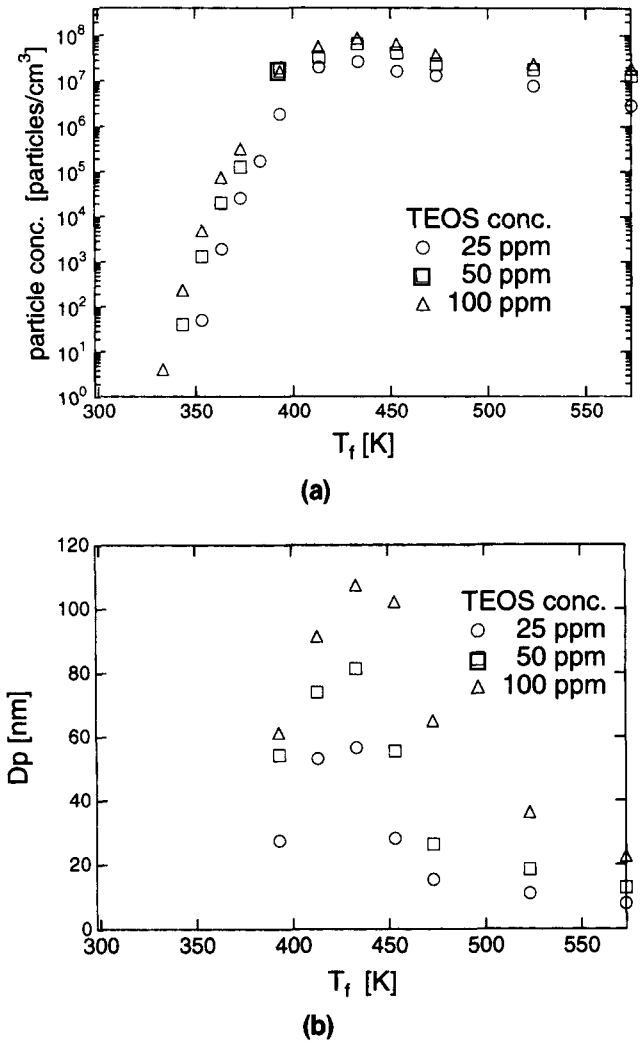

Figure 7. (a) Measured number concentrations and (b) mean volume diameters of particles at various temperatures.

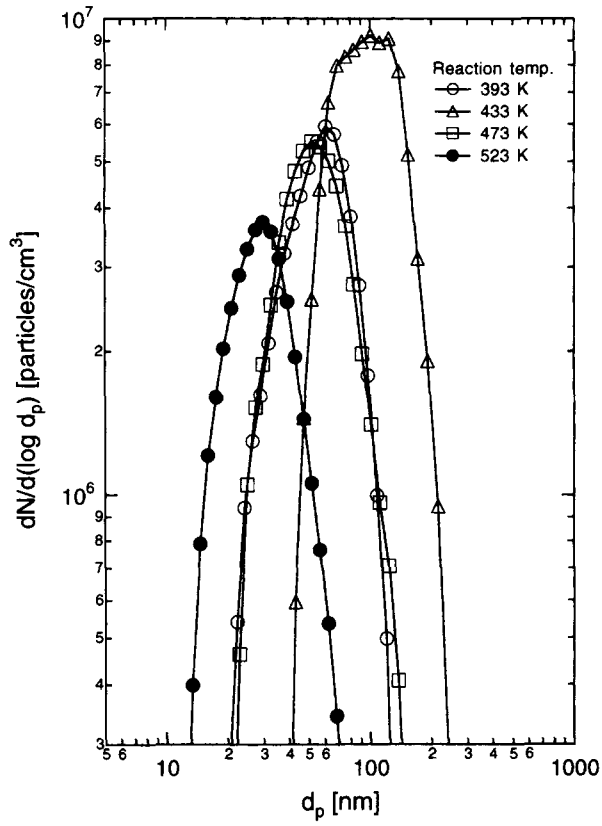

Figure 8. Change in particle-size distribution with reactor temperature.

Particle generation conditions at $C_{TEOS} = 2.04 \times 10^{-6}$ mol/L (50 ppm), $C_{O_3} = 4.25 \times 10^{-5}$ mol/L (1,040 ppm), $Q = 400$ cm^3/min, and $R_T = 6.5$ mm.

In a previous article, we reported on characteristics of particles formed in this system (Adachi et al., 1993). Particles were found from TEM observations to be amorphous with diameters ranging from 10–50 nm diameter. FT-IR spectra of the particles showed that a main component was SiO_2. As with films formed by APCVD of TEOS/O_3, small amounts of H_2O and the ethoxy group were also found.

Considering these features of particle generation in TEOS/O_3 APCVD processes, we made a model based on the following assumptions:

(1) Gas-phase intermediates species are formed by the gas-phase reaction of TEOS and oxygen radicals. These are the monomers for cluster and particle growth.

(2) The clusters and particles grow mainly by Brownian coagulation.

(3) The agglomerated particles are spheres.

(4) The density of the particle is equal to the density of TEOS.

(5) All of the particles hitting the reactor wall are removed from the gas phase.

Formation rate of intermediates

Many researchers have examined the chemical reaction kinetics of TEOS/O_3 APCVD and reached the following conclusions:

(1) TEOS reacts with oxygen radical but not with O_3 (Matsuura et al., 1991; Kawahara et al., 1992).

(2) The TEOS-oxygen radical reaction produces oligomers of TEOS in the gas phase (Matsuura et al., 1991; Kawahara et al., 1992; Satake et al., 1994).

(3) The main gas-phase byproducts are ethylene, ethanol, carbon dioxide and water (Desu, 1987; Matsuura et al., 1991; Kawahara et al., 1992).

From the above, we assume that the gas-phase intermediates are oligomers of TEOS reaction products that these intermediates coagulate to form liquid-like droplets, and that these droplets polymerize to form spherical silica-like particles. We used the following overall reaction model with the assumption that byproducts such as C_2H_4 and C_2H_5OH were immediately oxidized by oxygen radicals

$$n\mathrm{Si(OC_2H_5)_4} + 12(n-1)\mathrm{O}\cdot \xrightarrow{k_4} \mathrm{Si}_n\mathrm{O}_{(n-1)}(\mathrm{OC_2H_5})_{2(n+1)} + 4(n-1)\mathrm{CO_2} + 5(n-1)\mathrm{H_2O}. \quad (22)$$

The generation rates of TEOS and intermediates are expressed as

$$r_{TEOS} = -k_4 C_{TEOS} C_O, \qquad r_{inter} = k_4 C_{TEOS} C_O / n. \quad (23)$$

The net generation rate of the oxygen radical is then

$$r_O = k_1 C_{O_3} C_M - k_2 C_{O_2} C_O C_M - k_3 C_{O_3} C_O - 12(n-1) k_4 C_O C_{TEOS}. \quad (24)$$

The effect of the TEOS vapor on the thermal decomposition of ozone has not been previously studied. The coefficients in Eq. 15 were obtained experimentally in the absence of TEOS vapor. In this study, the TEOS concentration is less than 100 ppm, which is considerably lower than the concentrations of O_2 or N_2. Accordingly, we assume that TEOS plays an insignificant role as a third body in the decomposition of ozone.

Because of the oxygen radical's high reactivity and low concentration, the pseudo steady-state approximation was used to determination its concentration from Eq. 24

$$C_O = \frac{k_1 C_{O_3}}{k_2 C_{O_2} + k_3 C_{O_3}/C_M + 12(n-1) k_4 C_{TEOS}/C_M}. \quad (25)$$

Unfortunately, the reaction rate constant k_4 is unknown. However, because $C_{O_3}/C_M \ll 1$ and $C_{TEOS}/C_M \ll 1$, Eq. 25 can be simplified to

$$C_O \approx \frac{k_1 C_{O_3}}{k_2 C_{O_2}}. \quad (26)$$

To confirm this simplification we compared the value of C_O obtained with Eq. 25 with the value obtained with Eq. 26 using the rate constant k_4, which was determined later. The result shows that the simplified expression is valid at temperatures below 370 K.

The generation rate of intermediates r_{inter} can then be described as

$$r_{inter} = \frac{k_4 C_O C_{TEOS}}{n} = \frac{k_1 k_4 C_{O_3}}{n k_2 C_{O_2}} C_{TEOS} = \frac{k_{1_0} k_{4_0} C_{O_3} C_{TEOS}}{n k_{2_0} C_{O_2}} \times \exp\left[-\left(\Delta E_{k_4} + 1.00 \times 10^5 + 3.73 \times 10^3\right)/RT\right], \quad (27)$$

where k_{1_0}, k_{2_0}, and k_{4_0} are the frequency factors for k_1, k_2, and k_4, respectively. At low temperatures, the thermal decomposition rate of ozone and the consumption of TEOS can be ignored, so that the generation of intermediates is only a function of the temperature. Moreover, the concentration of particles is low enough that we can ignore the effect of coagulation. Therefore, the rate at which intermediates are generated is proportional to the rate of particle generation. Therefore, we can estimate the activation energy for the reaction between TEOS and oxygen radicals from the relationship between the furnace temperature and the particle concentration.

Arrhenius plots for particle number concentrations at TEOS concentrations of 25, 50 and 100 ppm, and reactor tube diameters of 13, 20 and 30 mm are shown in Figure 9. At temperatures below 370 K, $\Delta E/R$ for all cases is nearly

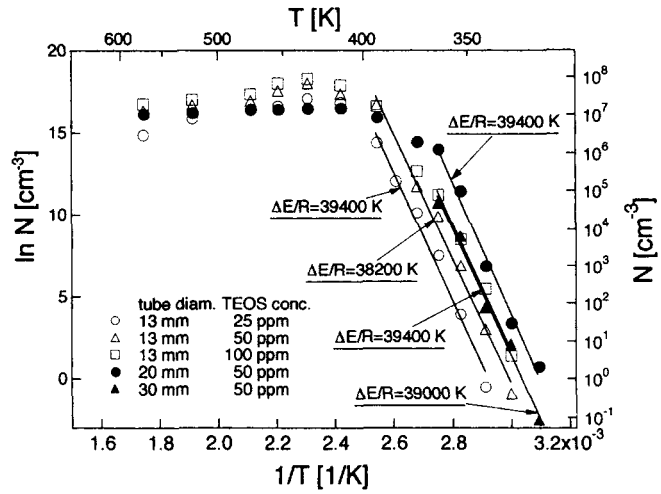

Figure 9. Measured particle number concentration on Arrhenius plot.

constant at 39,000 K. The observation that $\Delta E/R$ does not depend on the reactor tube diameter supports the argument that wall reactions do not affect concentrations of the intermediates.

From Eq. 27, the activation energy of the TEOS-oxygen radical reaction is 2.18×10^5 J/mol. From our experiments, however, we could not determine the frequency factor k_{4_0} of the reaction, so it was varied in the numerical simulations to get good agreement with experimentally observed particle concentrations.

Generation and growth rate of particles

The formation and growth rate of particles are governed by the so-called general dynamic equation of aerosols. In this study, we used the simplified reaction-coagulation (SRC) model. In the SRC model, as illustrated in Figure 10, the particle-size distribution is represented by a number of discrete sizes corresponding to the cluster size distribution, and a single average particle size that represents the size distribu-

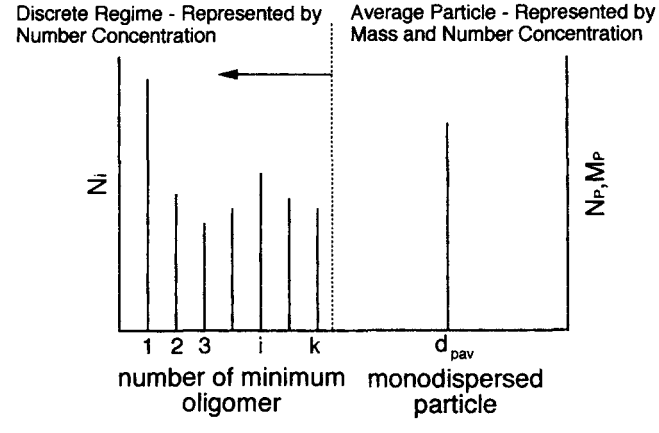

Figure 10. Particle-size spectrum used in the SRC model.

tion of larger particles. Material is added to the clusters from the reaction source and are transferred to the larger particle mode either when the clusters grow outside the discrete regime, or when they collide with the particles in the larger mode. The SRC model computes the number concentration of each discrete size N_l; the average particle size of the larger mode is calculated from the total number and mass concentration of the particles, N_p and M_p, respectively.

With this model, and introducing a term for particle formation in the diffusion equation, the change in the number concentration of monomers [that is, oligomers of TEOS; $Si_nO_{(n-1)}(OC_2H_5)_{2(n+1)}$] in the model is given by

$$\nabla\cdot D_1\nabla\left(\frac{N_1}{\rho}\right)-\nabla\cdot(\boldsymbol{u}+\boldsymbol{u}_{\text{th}})\left(\frac{N_1}{\rho}\right)-\rho\sum_{j=1}^{k}\beta_{1,j}\frac{N_1}{\rho}\frac{N_j}{\rho}-\rho\beta_{1,p}\frac{N_1}{\rho}\frac{N_p}{\rho}+\frac{N_{AV}\times10^3}{\rho}r_{\text{inter}}=0, \quad (28)$$

where D_l, N_{AV} and r_{inter} are the diffusion coefficient (m^2/s) of the monomer, Avogadro's number, and the generation rate of intermediates due to chemical reactions, respectively. β is the Brownian coagulation rate function for two particles (m^3/s).

The number concentration of an l-mer, consisting of l monomers, is expressed as

$$\nabla\cdot D_l\nabla\left(\frac{N_l}{\rho}\right)-\nabla\cdot(\boldsymbol{u}+\boldsymbol{u}_{\text{th}})\left(\frac{N_l}{\rho}\right)+\frac{1}{2}\rho\sum_{j=1}^{l-1}\beta_{l-j,j}\frac{N_{l-j}}{\rho}\frac{N_j}{\rho}-\rho\sum_{j=1}^{k}\beta_{l,j}\frac{N_l}{\rho}\frac{N_j}{\rho}-\beta_{l,p}\frac{N_l}{\rho}\frac{N_p}{\rho}=0. \quad (29)$$

The number concentration of the monodispersed particle distribution is expressed as

$$\nabla\cdot D_p\nabla\left(\frac{N_p}{\rho}\right)-\nabla\cdot(\boldsymbol{u}+\boldsymbol{u}_{\text{th}})\left(\frac{N_p}{\rho}\right)+\frac{1}{2}\rho\sum_{i=1}^{k}\sum_{j=1}^{k}\beta_{k+i-j,j}\frac{N_{k+i-j}}{\rho}\frac{N_j}{\rho}-\frac{1}{2}\rho\beta_{p,p}\left(\frac{N_p}{\rho}\right)^2=0. \quad (30)$$

The mass concentration of the monodisperse particle distribution is expressed as

$$\nabla\cdot D_p\nabla\left(\frac{M_p}{\rho}\right)-\nabla\cdot(\boldsymbol{u}+\boldsymbol{u}_{\text{th}})\left(\frac{M_p}{\rho}\right)+\frac{1}{2}\rho\sum_{i=1}^{k}\sum_{j=1}^{k}m_{k+i}\beta_{k+i-j,j}\times\frac{N_{k+i-j}}{\rho}\frac{N_j}{\rho}+\sum_{j=1}^{k}m_j\beta_{j,p}\frac{N_j}{\rho}\frac{N_p}{\rho}=0 \quad (31)$$

where the average volume of a particle is expressed as

$$v_p=\frac{M_p}{\rho_p N_p} \quad (32)$$

where M_p is the mass concentration of the average particle (kg-particle/m^3), ρ_p is the density of the particle (kg/m^3), and v_p is the volume of the single particle (m^3).

Assuming that the particles are spherical, the average diameter of the particles d_p (m) is

$$d_p=\left(\frac{6v_p}{\pi}\right)^{1/3}=\left(\frac{6M_p}{\pi\rho_p N_p}\right)^{1/3}. \quad (33)$$

The coagulation coefficient of two particles of diameters $d_{p,i}$ and $d_{p,j}$ in Eqs. 28 to 33 is given by the Fuchs interpolation formula (Fuchs, 1964). Thermophoretic velocity, $\boldsymbol{u}_{\text{th}}$ (m/s) is expressed as (Talbot et al., 1980)

$$u_{\text{th}}=-K_T\frac{\mu}{\rho}\nabla(\ln T), \quad (34)$$

$$K_T=\frac{2.294[(k_g/k_p)+2.20Kn]\{1+Kn[1.2+0.41\exp(-0.88/Kn)]\}}{(1+3.438Kn)[1+2(k_g/k_p)+4.40Kn]}, \quad (35)$$

where m, K_T, k_g, k_p and Kn are the viscosity of the carrier gas, the thermophoretic coefficient, the thermal conductivity of carrier gas (W/(m·K)) and particles (W/(m·K)), and the Knudsen number, respectively. Because the thermal conductivity of the intermediates is unknown, we assume it is equal to that of silica.

The number of clusters considered in the discrete regime size k is 10. The model provides the same results when $k=20$ indicates that more accurate results would not be obtained by using a larger value of k. The number of TEOS molecules in a unit oligomer [that is, $Si_nO_{(n-1)}(OC_2H_5)_{2(n+1)}$] n was 2.

Figure 11a shows the number concentration of particles generated at various temperatures. For the experimental measurements, the initial ozone concentration was kept at 4.25×10^{-5} mol/L and the TEOS concentration was set to 25, 50 and 100 ppm. The frequency factor k_{4_0}, used in this calculation was 1.0×10^{39} L/(mol·s). The corresponding average particle diameter is shown in Figure 11b. The number concentration and particle size are proportional to the TEOS concentration. Numerical results for particle number concentrations agree well with the experimental results. A small disagreement is seen at temperatures above 450 K. This decrease may result from particle deposition on the reactor walls because the diffusion coefficient increases as the particle size decreases. Calculated results for particle size, agree well with experimental results at temperatures below 430 K, but do not explain the reduction of measured particle size at higher temperatures.

To probe the reduction of particle size at higher temperatures, thermal desorption spectra (TDS) of the particles were measured. The TDS apparatus (Denshi Kagaku Co. Ltd.,

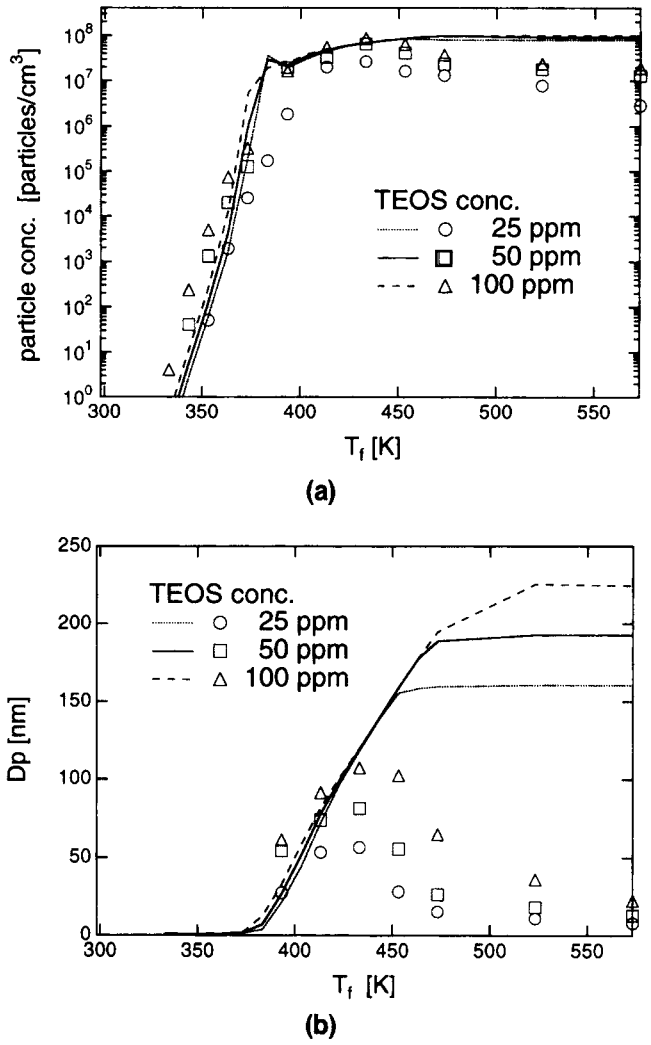

Figure 11. Measured vs. calculated (a) number concentration and (b) mean volume diameter of particles.

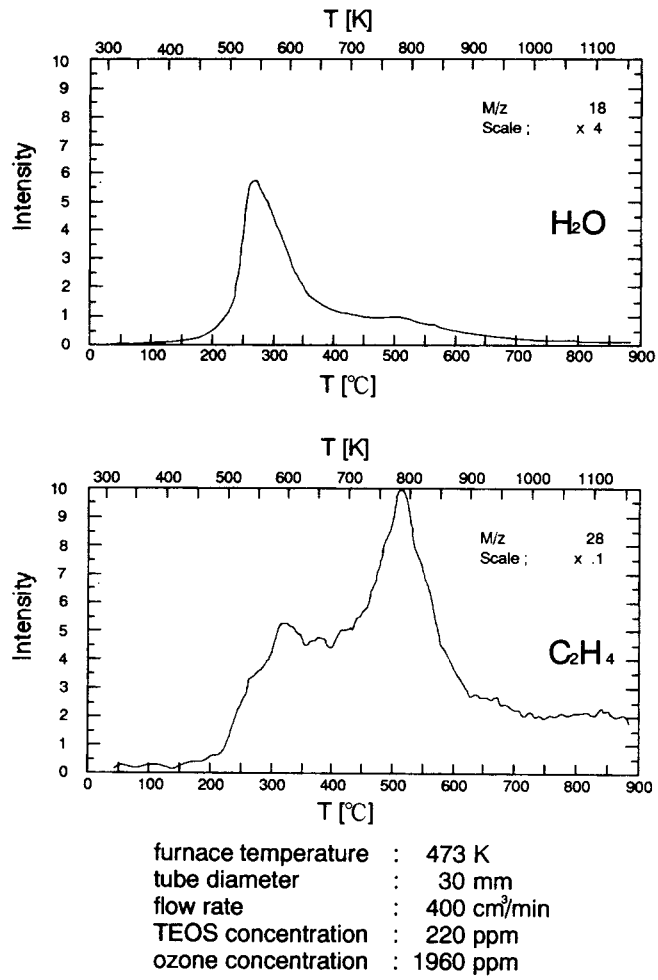

Figure 12. Thermal desorption spectra of H_2O and C_2H_4 for nanometer-size particles.

$T_f = 423$ K, $C_{TEOS} = 8.98 \times 10^{-6}$ mol/L (220 ppm), $C_{O_3} = 8.01 \times 10^{-5}$ mol/L (1,960 ppm), $Q = 400$ cm^3/min, and $R_T = 15$ mm.

EMD-WA1000) has previously been used to measure outgassing from TEOS/O_3-APCVD films. Particulate samples to be analyzed by TDS were captured on Si wafers in the electrostatic precipitator at the reactor outlet. The sample wafers were transferred and placed into the TDS apparatus under a N_2 atmosphere. The pressure in the TDS analysis chamber was then reduced to 10^{-9} torr so as to avoid contact with atmospheric air. FT-IR spectra of the condensable material collected in the liquid-nitrogen trap showed significant amounts of the water (Adachi et al., 1995). The water in the TDS spectra of the particles therefore came from particles and not from atmospheric contamination.

Figure 12 shows TDS spectra for mass fragments with *M/Z* of 18 (H_2O) and 28 (C_2H_4) from particles generated at a temperature of 423 K. In the spectrum for H_2O, a primary peak at 300°C and shoulder at 500°C were observed. These peaks suggest that H_2O is produced from a hydroxyl group (-OH) by a β-elimination reaction. Peaks of C_2H_4 were observed at 300°C and 530°C. The peak at 300°C is associated with N_2 gas used during the TDS measurement. The peak at 530°C represents C_2H_4 generated from the ethoxy group (C_2H_5O-). The emission of C_2H_4 from the particles suggests that the disagreement between the experimental and numerical results shown in Figure 11 was due, at least in part, to the shrinkage of particles by β-elimination reactions of ethoxy groups.

Conclusions

Continuity, momentum, and energy conservation equations were solved simultaneously with the convective-diffusion equations to simulate thermal decomposition of ozone in a tube reactor. Good agreement between experimental and numerical results validate the extension to flow reactors of the well known mechanisms and rate constants for the thermal decomposition of ozone obtained using batch reactors.

From measurements of particle generation at low temperature, the activation energy was obtained and was independent of the reactor diameter. This result suggests that particle formation is not affected by surface reactions on the reactor wall.

The aerosol general dynamic equations were solved together with expressions for the thermal decomposition of

ozone in a tube reactor. The numerical results agreed with the experimental results for the particle number concentration. For particle size, the calculated results agree well with experimental results at temperatures below 430 K, but do not explain the reduction of measured particle size at higher temperatures. Using TDS spectra, we conclude that the reduction of particle diameter at high temperature is due, at least in part, to the shrinkage of particles by β-elimination reactions of the ethoxy group.

Acknowledgment

This work was supported in part by grant from the CVD Project Research of the Society of Chemical Engineers, Japan and the Chugoku Electric Power Co., Inc. and grants-in-aid for Developmental Scientific Research from the Ministry of Education, Science, Sports and Culture (Nos. 05239207, 05650769, 07555235, 07650927 and 08305033), the Proposal-Based Advanced Industrial Technology R&D Program of NEDO (C-1111), "Research for the Future" of the Japan Society for the Promotion of Science (96P00402), and JSPS Research Fellowships for Young Scientists (3685).

Notation

m = mass of single particle, kg
m_g = weight of gas molecule, kg
N = number concentration of particle, particles/m^3
p = pressure of carrier gas, Pa
R = gas constant, 8.31 J/(mol·K)
ΔE_{k4} = activation energy, J/mol
μ = viscosity of carrier gas, Pa·s
τ = shear stress, N/m^2

Subscripts

i, j, l = cluster number in discrete size spectrum

Literature Cited

Adachi, M., K. Okuyama, N. Tohge, M. Shimada, J. Sato, and M. Muroyama, "Gas-Phase Nucleation in an Atmospheric Pressure Chemical Vapor Deposition Process for SiO_2 Films Using Tetraethylorthosilicate (TEOS)," *Jpn. J. Appl. Phys.*, **31**, L1439 (1992).

Adachi, M., K. Okuyama, N. Tohge, M. Shimada, J. Sato, and M. Muroyama, "Particle Generation and Film Formation in an Atmospheric-Pressure Chemical Vapor Deposition Reactor Using the Tetraethylorthosilicate (TEOS)/He, TEOS/O_2/He and TEOS/O_3/He Systems," *Jpn. J. Appl. Phys.*, **32**, L748 (1993).

Adachi, M., K. Okuyama, N. Tohge, M. Shimada, J. Sato, and M. Muroyama, "Precursors in Atmospheric-Pressure Chemical Vapor Deposition of Silica Films from Tetraethylorthosilicate/Ozone System," *Jpn. J. Appl. Phys.*, **33**, L447 (1994).

Adachi, M., K. Okuyama, and N. Tohge, "Particle Generation and Film Formation in an Atmospheric-Pressure Chemical Vapour Deposition Process using Tetraethylorthosilicate," *J. Mat. Sci.*, **30**, 932 (1995).

Adachi, M., T. Fujimoto, K. Okuyama, J. Sato, and M. Muroyama, "Morphology Control of Films Formed by Atmospheric-Pressure Chemical Vapor Deposition Using Tetraethylorthosilicate/Ozone System," *Jpn. J. Appl. Phys.*, **35**, 284 (1996).

Adams, A. C., and C. D. Capio, "The Deposition of Silicon Dioxide Films at Reduce Pressure," *J. Electrochem. Soc.*, **126**, 1042 (1979).

Benson, S. W., and A. E. Axworthy, "Mechanism of the Gas Phase, Thermal Decomposition of Ozone," *J. Chem. Phys.*, **26**, 1718 (1957).

Benson, S. W., and A. E. Axworthy, "Reconsideration of the Rate Constants from the Thermal Decomposition of Ozone," *J. Chem. Phys.*, **42**, 2614 (1965).

Desu, S. B., "Decomposition Chemical of Tetraethoxysilane," *J. Amer. Ceram. Soc.*, **72**, 1615 (1987).

Fuchs, N. A., *The Mechanics of Aerosol*, Pergamon Press, Oxford (1964).

Fujino, K., Y. Nishimoto, N. Tokumasu, and K. Maeda, "Dependence of Deposition Characteristics on Base Materials in TEOS and Ozone CVD at Atmospheric Pressure," *J. Electrochem. Soc.*, **137**, 2883 (1990).

Fujino, K., Y. Nishimoto, N. Tokumasu, and K. Maeda, "Silicon Dioxide Deposition by Atmospheric Pressure and Low-Temperature CVD Using TEOS and Ozone," *J. Electrochem. Soc.*, **138**, 550 (1991).

Fujino, K., Y. Nishimoto, N. Tokumasu, and K. Maeda, "Modification of Base Materials for TEOS/O_3 Atmospheric Pressure and Chemical Vapor Deposition," *J. Electrochem. Soc.*, **139**, 1690 (1992).

Gelbard, F., and J. H. Seinfeld, "The General Dynamic Equation of Aerosol," *J. Colloid Interf. Sci.*, **68**, 363 (1979).

Kawahara, T., A. Yuuki, and Y. Matsui, "Reaction Mechanism of Chemical Vapor Deposition Using Tetraethylorthosilicate and Ozone at Atmospheric Pressure," *Jpn. J. Appl. Phys.*, **31**, 2925 (1992).

Matsuura, M., Y. Hayashide, H. Kotani, and H. Abe, "Film Characteristic of APCVD Oxide Using Organic Silicon and Ozone," *Jpn. J. Appl. Phys.*, **30**, 1530 (1991).

Okuyama, K., Y. Kousaka, N. Tohge, S. Yamamoto, J. J. Wu, R. C. Flagan, and J. H. Seinfeld, "Production of Ultrafine Metal Oxide Aerosol Particles by Thermal Decomposition of Metal Alkoxide Vapors," *AIChE J.*, **32**, 2110 (1986).

Okuyama, K., R. Ushio, Y. Kousaka, R. C. Flagan, and J. H. Seinfeld, "Particle Generation in Chemical Vapor Deposition Process with Seed Particles," *AIChE J.*, **36**, 409 (1990).

Okuyama, K., D. Huang, J. H. Seinfeld, N. Tani, and Y. Kousaka, "Aerosol Formation by Rapid Nucleation During the Preparation of SiO_2 Thin Films from $SiCl_4$ and O_2 Gases by CVD Process," *Chem. Eng. Sci.*, **46**, 1545 (1991).

Patankar, S. V., *Numerical Heat Transfer and Fluid Flow*, McGraw-Hill, New York (1980).

Satake, T., T. Sorita, H. Fujioka, H. Adachi, and H. Nakajima, "Detection of Intermediates in Thermal Chemical Vapor Deposition Process Using Tetraethoxysilane," *Jpn. J. Appl. Phys.*, **33**, 3339 (1994).

Talbot, L., R. K. Cheng, R. W. Schafer, and D. R. Willis, "Thermophoresis of Particles in a Heated Boundary Layer," *J. Fluid Mech.*, **101**, 737 (1980).

Whitby, E. R., and M. Hoshino, "Particle Size Distribution in a Low-Pressure SiH_4:O_2:H_2 CVD Reactor: Experimental and Numerical Results," *J. Electrochem. Soc.*, **143**, 3397 (1996).

Wu, J. J., and R. C. Flagan, "A Discrete-Sectional Solution to the Aerosol Dynamic Equation," *J. Colloid Interface Sci.*, **123**, 339 (1988).

Wu, J. J., H. V. Nguyen, R. C. Flagan, K. Okuyama, and Y. Kousaka, "Evaluation and Control of Particle Properties in Aerosol Reactors," *AIChE J.*, **34**, 1249 (1988).

Manuscript received Oct. 28, 1996, and revision received May 5, 1997.